ORIGINAL PAPER

Enhanced lithological mapping of Durba-Araba basement blocks, along the eastern margin of the Central Gulf of Suez Rift, Egypt, using Landsat-8 Data

Adel M. Seleim[1] · Mahmoud H. Bekiet[1] · Mohamed S. Hammed[2]

Abstract

The eastern margin of the central Gulf of Suez rift exposes unique rotated basement blocks of Gabal Durba-Araba. According to geological maps, these blocks are composed of Dokhan volcanic, older, and younger granites cut by basaltic dikes and overlayed by a tilted sedimentary succession of Paleozoic to quaternary. Herein, we propose a workflow of stepwise preprocessing and classification procedures for Landsat-8 (OLI) data verified by control points from previous maps to update and improve lithological discrimination in converging areas that require further field mapping. The workflow applies digital image-processing techniques, including spectral signature analysis, band-ratio transformation, maximum likelihood, and Mahalanobis supervised classifications. The accuracy assessment of the lithological mapping reaches 86.6% and 75.7% for maximum likelihood and Mahalanobis classifications, respectively. By running the Tactical Hyperspectral Operations Resource (THOR) algorithm on the classified images, we could accurately map and modify the lithological boundaries for the following rock units: (1) gneiss-amphibolite-schist, tonalite, and granodiorite at Gabal Araba; (2) granitic gneiss, granodiorite, biotite-muscovite-leucogranite, and riebeckite-syenite-albitite at Gabal Abu Haswa; (3) Dokhan volcanic, granite biotite-muscovite-leucogranite, granites riebeckite-syenite-albitite, Pyroclastic breccia and lava flow, and NW tertiary dike at Gabal Abu Durba.

Introduction

The Gulf of Suez rift is a significant geological province with a long history of oil and gas production and mining exploration. Its Neogene opening led to the development of several tilted fault blocks with three transverse provinces (north, central, and southern province;

✉ Adel M. Seleim
  Adelgeo2005@azhar.edu.eg

  Mahmoud H. Bekiet
  mahmoud.bekiet1960@gmail.com

  Mohamed S. Hammed
  salehhammed@cu.edu.eg

[1] Geology Department, Faculty of Sciences, Al-Azhar University, 11751 Nasar City Cairo, Egypt

[2] Geology Department, Faculty of Science, Cairo University, Giza 12613, Egypt

Moustafa 1976). For a long time, the unique exposures of the rotated basement block structures and stratigraphy on both sides of the Gulf of Suez have attracted geologists worldwide (Ungerer et al. 1984; Montenat et al. 1988; Moustafa and El-Raey 1993; Abdelkareem et al. 2021). The study area contains three exposed rotational fault blocks cored with the Neoproterozoic basement. The basement cores (including Gebel El Zeit and Esh El Malaha on the southwestern margin and Gabal Durba-Araba on the central-eastern margin) represent a surface analog model for the unconventional subsurface basement reservoir in the rift area. There is a need for detailed mapping of the basement cores to understand their subsurface extensions and discover new areas suitable for energy and mineral development.

In arid and semi-arid environments, as the study area, remote sensing datasets and their superior technology are effective for geological mapping due to the exposed bedrock and lack of soil or vegetation coverage (Elhebiry et al. 2020; Abdelaal et al. 2021). Owing to their

Table 1 The Characteristics of spectral bands of Landsat-8 (OLI)

Sensor	Subsystem	Band Number	Spectral Range (μm)	Ground resolution (m)	Swath width (Km)	Year of Launch
Landsat-8 (OLI)	VNIR	PAN (8)	0.500–0.680	15	185	2013
		Costal aerosol (1)	0.433–0.453	30		
		Blue (2)	0.450–0.515			
		Green (3)	0.425–0.600			
		Red (4)	0.630–0.680			
		NIR (5)	0.845–0.885			
	SWIR	SWIR 1 (6)	1.560–1.660			
		SWIR 2 (7)	2.100–2.300			
		Cirrus (9)	1.360–1.390			
	TIR	TIRS 1 (10)	10.60–11.19	100		
		TIRS 2 (11)	11.50–12.51			

spatial, spectral, and radiometric properties, remote sensing techniques are efficient in lithological mapping. The digital format of remote sensing data enables advanced image processing techniques, which, in turn, enhance the extraction of information for mapping (Ghrefat et al. 2021). Remote sensing is a significant tool for tracing lithological boundaries, and it is widely used in regional and detailed mapping, geomorphological and structural interpretation, and mineral prospecting (Crosta 1989; Hassan et al. 2015; Hassan and Sadek 2017; Zakeri et al. 2017; Gaber et al. 2017; Beiranvand Pour et al. 2018; Abu El-Leil et al. 2019; Rajan Girija and Mayappan 2019; Hamimi et al. 2020; Abdelkareem et al. 2021). The progress made so far in the optical Landsat-8 (OLI) data is appropriate for remote lithological mapping and reducing the cost and time of field surveys and displays an array of multispectral data spanning a large area (Zhu and Abdelkareem 2021). The use of the Landsat-8 OLI multispectral dataset enhances structural, lithologic, and geomorphic remote sensing mapping (El-Din and Abdelkareem 2018; Abdelkareem et al. 2020). It comprises high radiometric resolution (16 bits) that covers a wide spectrum of nine spectral bands with a spatial resolution of 30 m for bands 1–7 and 9 divided into shortwave infrared (SWIR), thermal infrared (TIR), and visible segments (Table 1).

Employing remote sensing techniques and field verification, Seleim and Hammed (2016) and Abdelkareem et al. (2021) provided a detailed lithological map for southwestern rotated blocks in the Gulf of Suez rift. Most studies on the rotated basement blocks of Gabel Durba-Araba were based on field observations, geochemistry, and geochronology sampling (e.g., Egyptian Geological Survey 1994; El-Bialy 1999; Anbar et al. 2005; and Geological Survey 2015). These mapping attempts produced large-scale maps (Egyptian Geological Survey

1994; Geological Survey 2015), yet military restrictions and limited accessibility hindered sample collection from the study area. Lithological mapping depending solely on regional field surveys and geochemical analysis assisted with aerial photos of low spatial resolution results in geological maps with poorly defined boundaries (e.g., Eyal and Hezkiyahu 1980; Gharib and Obeid 2004; Azer 2006). Thus, there is a need to discriminate rock units and accurately define their contacts by applying remote sensing techniques using high-resolution satellite datasets.

The study area is a part of the Afro-Arabian Nubian Shield, which was intensively mapped using various remote sensing sensors and field verified (El-Din and Abdelkareem 2018; Abu El-Leil et al. 2019; Asran and Hassan 2021; Shokry et al. 2021). The efficiency of OLI sensors in lithological discrimination has been tested and validated in the same terrain (Seleim and Hammed 2016). Therefore, in this study, we employed advanced image processing techniques on multispectral OLI datasets to enhance previous maps and differentiate the lithologies of Gabal Durba-Araba (Fig. 1). The following techniques were used in this study:

1. Optimum Index Factor (OIF), a statistical approach widely used to define the most advantageous three-band combinations (Qaid and Basavarajappa 2008)
2. Band composite image
3. Detailed spectral signature analysis for material identification and characterization (Govender et al. 2007)
4. Band rationing (BR), which has been widely used for mapping mineral abundance from multispectral Landsat datasets (San et al. 2004). In this study, BR was created from pixel reflectance instead of the digital number (DN), which is a more related characteristic of identified rock units
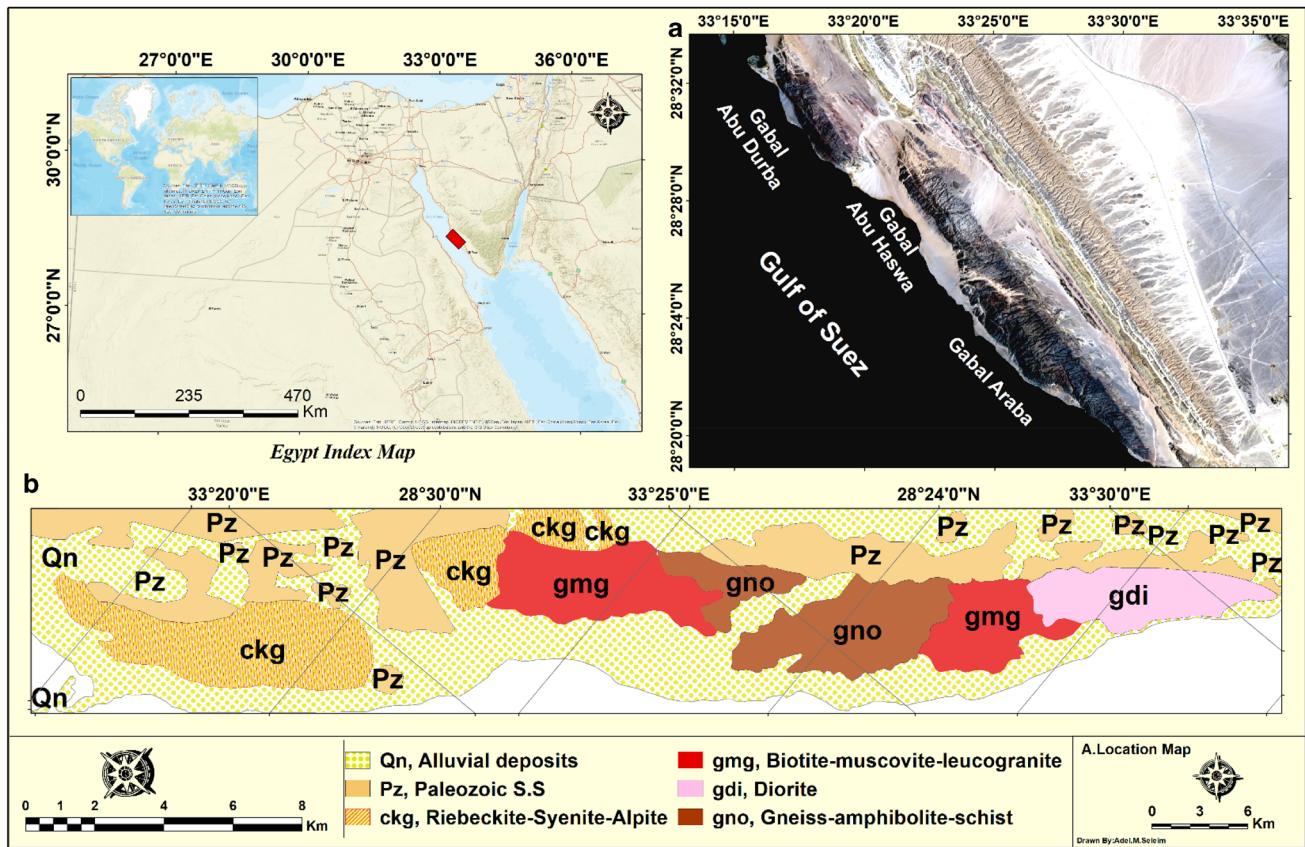
Fig. 1 **a** Optical Landsat-8 (RGB; 4 3 2) image shows the locations of the study area with reference to Egypt map; **b** geological map of Egypt, the study area showing the location of different types of lithological rock units

5. Tactical Hyperspectral Operations Resource (THOR) for material identification, which is a robust tool for discriminating land surface features and landscape patterns (THOR was applied for the first time in the study area for rock units that have a controversy on the previously published maps)

6. Supervised image classification techniques, such as maximum likelihood and Mahalanobis distance. Based on the results of the proposed workflow of these processing techniques, we could accurately map the lithological boundaries between different rock units.

Geological setting

The Pan-African basement subsegments of granitoid, volcanic, and dikes are exposed in the central part of the Gulf of Suez named from north to south Gabal Durba, Gabal Abu Haswa, and Gabal Araba (Fig. 1a). Egyptian Geological Survey (1994) classified the Neoproterozoic of Gabal Durba-Araba into four rock units, and Gabal Araba was divided into gneiss–amphibolite–Schist, tonalite,

diorite, granodiorite, and biotite-muscovite-leucogranite. Gabal Abu Haswa is classified into two (biotite-muscovite-leucogranite and riebeckite-syenite-albitite), and Gabal Durba is classified as one rock unit of granite riebeckite-syenite-albitite (Fig. 1b). The basement rocks of Abu Durba Abu Haswa comprise the following rock units: older granites, phase II younger granites, phase III younger granites, post-granitic dykes, acidic porphyries, pyroclastic, and lava flow of tertiary basalts (El-Bialy 1999). Fieldwork and petrography reported by Anbar et al. (2005) indicate that the northern part of Gabal Abu Durba is occupied by phase II younger granites (granodiorites), intrudes into volcanics of the Dokhan type, and sends off-shoots and apophyses into the Dokhan volcanic. The Dokhan volcanic and younger granites are dissected by post-granite basic dikes of tertiary age trending NW. The phase III younger granites (monzogranites) located at the south-eastern part of Gabal Abu Durba intrude into volcano of the Dokhan type. The Gabal Abu Haswa, on the other hand, is composed mainly of phase II younger granites (granodiorites), which are intruded by phase III younger granites (monzogranites and alkali feldspar granites). Geological and Survey 2015 divided the basement

rocks of Gabal Durba into syenogranite and volcanic breccia and post granitic olivine basalt dikes, and Gabal Abu Haswa was divided into granitic gneiss. Gabal Araba is occupied by gneiss, amphibolite, schist, tonalite, diorite, granodiorite, and postgranitic olivine basalt dikes. The Neoproterozoic rocks of the Gebel Durba-Araba Fault block form two subblocks separated by NNE–SSW–oriented fault (Durba-Araba Fault) that marks the southern boundary of the Durba block and separates it from the Araba block lying south of them (Patton et al. 1994). The structure of the central-eastern margin of the Gulf of Suez is dominated by two main extensional fault systems: the rift bounding and coastal fault systems of the Durba-Araba Fault (Hammed 2002). The two faults are in the study area, and both are hard-linked normal fault segments in zigzag arrays and of two dominant strikes, Gulf parallel NW-trending and Gulf oblique NNE-trending faults (Morley 1995). The plain area between the two basement blocks is a sedimentary depocenter known as the El Qaa basin (Fig. 1a). The Durba-Araba Fault dips 65° NW and has oblique-slip displacement. It shows good evidence of drape folding of the overlying sedimentary section toward the NW as well as acceptable evidence of left-lateral strike-slip displacement. The Paleozoic sedimentary section juxtaposed against the Precambrian basement outcrop on the northern side of the fault has a NW dip of approximately 25° and indicates drape folding over the NW dipping surface of the fault. This sequence comprises a thick pre-rift section of the Paleozoic Lower Cretaceous clastic of Nubia sandstones, and Upper Cretaceous–Eocene mixed clastic and carbonates unconformably overlay the Precambrian basement (Abdallah and El-Adindani 1963).

Dataset and preprocessing

The approach used in this study updates the lithological map of the study region. The dataset was derived from a Landsat-8 scene (175/040) row, UTM projection of zone 36, and WGS-84 datum taken in October 2019 with scene ID "LC81750402019225LGN00." The data were obtained from the US Geological Survey (USGS). Many computational processes, such as data preparation, feature extraction, model construction, and model assessment, are required in modern data science. For land use/land cover mapping, even a simple correction method can give satisfactory results, providing pure pixels and spectral signatures corresponding to specific land cover types for classification (Chrysoulakis et al. 2010). Preprocessing steps are required to improve the dataset used in the compilation of a remote predictive lithological map of the study area, including layer stack, subset by

Table 2 Shows that the reflectance has negative values that are not within the normal range

Basic Stats	Min	Max	Mean	Stdev
Band 1	−6.895496	2.032601	0	1.483781
Band 2	−1.093676	0.905435	0	0.0498
Band 3	−0.377295	0.255065	0	0.01699
Band 4	−0.348717	0.15878	0	0.008303
Band 5	−0.198802	0.056709	0	0.005871
Band 6	−0.055629	0.129259	0	0.003922
Band 7	−0.048502	0.029695	0	0.00148

region of interest (ROI). Moreover, several procedures are necessary to prepare data for conversion from digital number (DN) to reflectance data, including masking the water band, radiometric correction, and fast line-of-sight atmospheric analysis of hypercube algorithm (FLAASH), which was used herein for atmospheric correction (Cooley et al. 2002). Some pixels may fall outside this range; they generally correlate to highly reflecting surfaces that cause saturation, or they might be dark, negative values seen in deep water or shadows. When the radiance is low, the reflectance values fall outside the normal range (Table 2). Hence, there is a need to rescale the radiance data, where the Band Math tool is used to divide the pixel values by 10,000 to convert them to floating-point values ranging from 0 to 1.0 using the post FLAASH equation (Matthew et al. 2000) for every 7 bands (Table 3):

$$(B1 \; le \; 0) \; * \; 0 + (B1 \; ge \; 10000) * 1 + (B1 \; gt \; 0 \; and \; B1 \; lt \; 10000)$$

$$* \; float \; (b1)/10000$$

Comparing images before and after FLAASH preprocessing, we find that the processed images are sharper and more accurate (Fig. 2).

Table 3 Illustrate the reflectance values range between 0-1 after rescaling radiance data

Basic Stats	Min	Max	Mean	Stdev
Band 1	0	0.4529	0.098158	0.081858
Band 2	0	0.472	0.104111	0.08739
Band 3	0	0.626	0.157825	0.131394
Band 4	0	0.7334	0.213685	0.176122
Band 5	0	0.8151	0.25269	0.208006
Band 6	0	0.495547	0.934788	0.590724
Band 7	0	0.2323	0.083441	0.067732

Fig. 2 Gabal Abu Haswa in band composite images 7 6 2 RGB above and 7 5 1 RGB below before (left) and after (right) FLAASH atmospheric correction
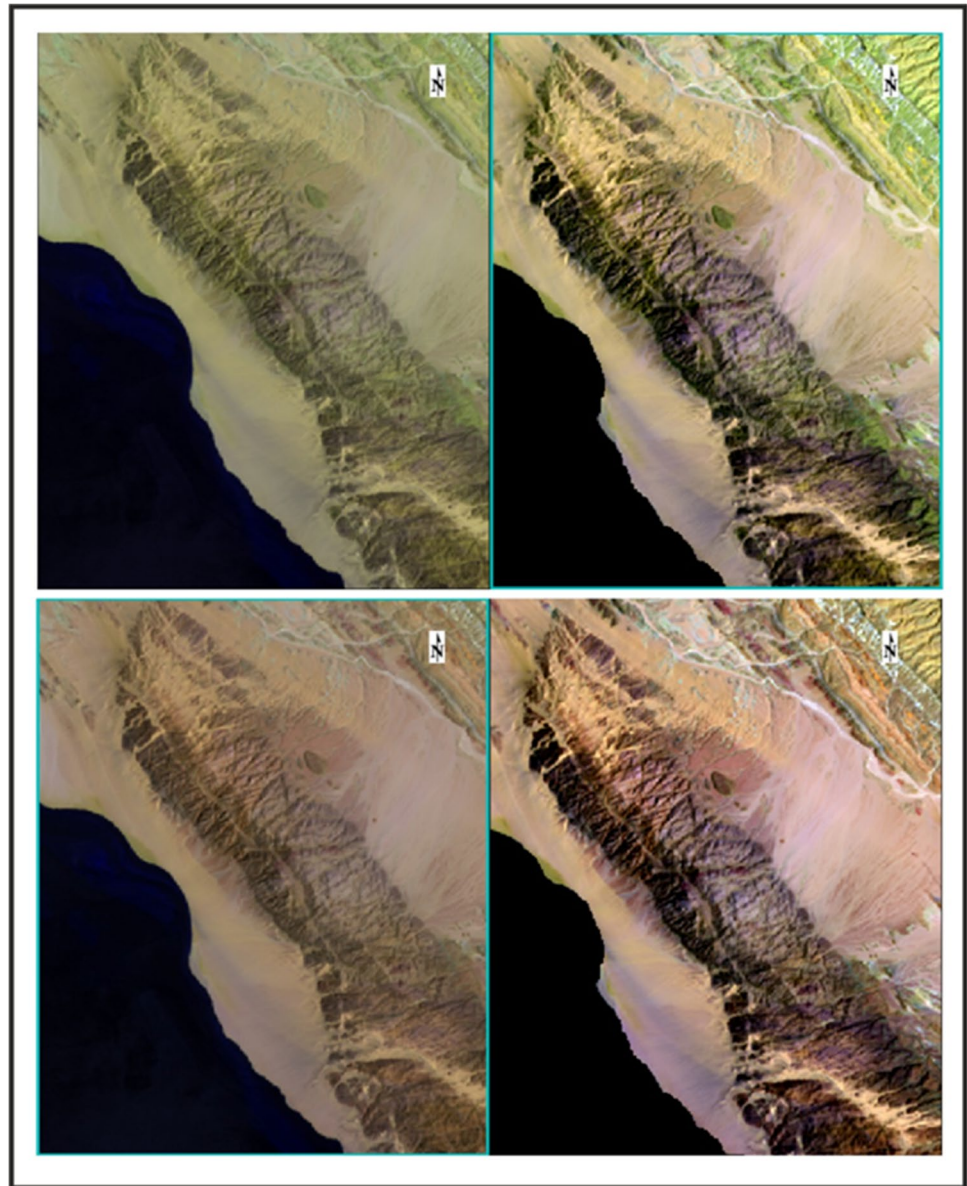
Data processing and methodology

The remote-sensing technique used in this work is described in detail in Fig. 3. It consists of seven major stages. (1) OIF was utilized to define the most beneficial three-band composite image. (2) Ban sharpening was performed. (3) The spectral signature for the image's different rock units was extracted using ENVI 5.3 software (Fig. 6). (4) The collected spectral signatures of the examined rock units were used as a guide to select the best spectral BR transformation images. (5) THOR was used for detecting unknown rock units in ENVI 5.3 software by comparing the target spectral signature to the reference spectral applied for the first time in the study area. (6) Supervised image classification was performed.

(7) All remote-sensing datasets and processing efforts in Sinai were verified by previously published geology and topography maps. ENVI 5.3, ESRI ArcGIS 10.5, and ILWIS software were used to perform image preprocessing and analysis (Fig. 3).

Color composite images

The satellite image, which appears in a distinct band as a black and white band, indicates a low and hazy contact between the lithological rock groups. When presented as red, green, and blue imagery, the comparison of spectral properties of land features in several bands (color composites) shows improved separation/contrast

Fig. 3 A summary of the methodological flowchart showing the characteristics used in this study and its characteristics of the image processing and analysis algorithm
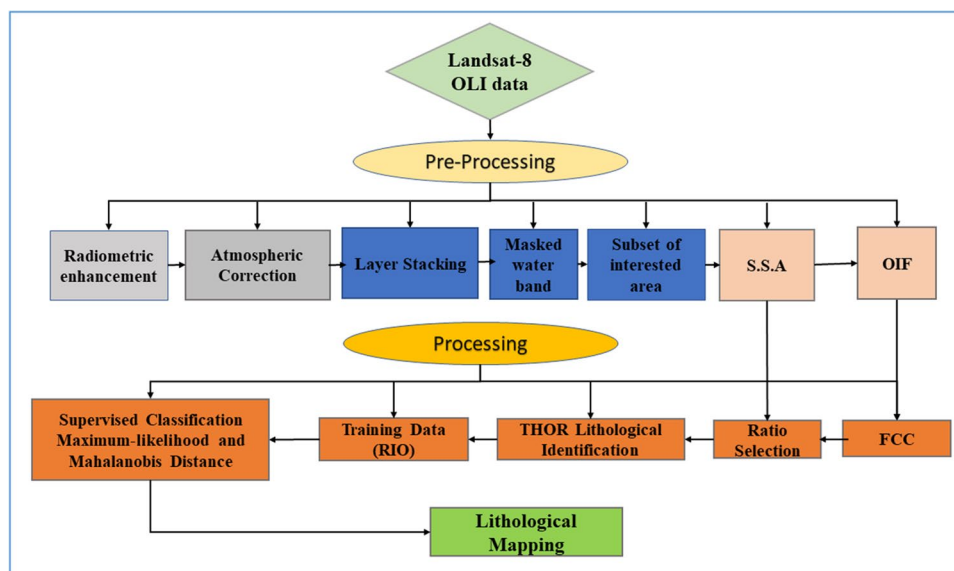

Table 4 List of the RGB and combination of five highest OIF % ranks for VNIR, and SWIR bands

Ranks	R	G	B	OIF %
1	B7	B6	B2	90.46
2	B7	B5	B1	88.28
3	B6	B5	B2	88.23
4	B6	B4	B1	87.47
5	B7	B4	B1	87.21

across distinct surfaces. In the case of Landsat-8, 4–3-2 RGB bands, the combination of the same spectral bands, such as the visible band, is a true-color composite image (Fig. 1a). When the image is merged between multiple spectral bands, it is referred to as a false-color composite (FCC), and it maintains its morphological characteristics and presents distinct lithological units in different hues (Al-Nahmi et al. 2016). Herein, we employed many FCC of the OLI band as 7, 6, 2 RGB and 7, 5, 1 RGB combination based on OIF to select the optimal band combination of Landsat OLI data using ELWIs 3.4 software (Table 4). Then, the images were used to extract the spectral signature of rock unit as they characterize different rock boundaries (Figs. 4 and 5).

Band ratio

BR is employed in remote sensing to efficiently depict spectral fluctuation and increase material contrast. It was easily applied by dividing the DN of each pixel in one band by that of another (Drury and Walker 1987; Sabine 1999). Depending on the research purpose, BR can also convey spectral or color information. Different forms of BR can be used for a range of purposes, such

as lithological mapping or alteration discrimination. The properties of image components change in scene light (Omwenga 2018). After eliminating the atmospheric state, several BR composite images were created using OLI data. Spectral band rationing is particularly effective for highlighting certain features or materials that are not visible in digital numerical data (Ourhzif et al. 2019).

In this study, the lithological map was enhanced by analyzing the Landsat-8 data to distinguish lithological rock units based on spectral characterization derived from band combinations of 7, 6, 2 RGB and 7, 5, 1 RGB data images.

The spectral contrast between the bands shows the following:

- A low reflectance characteristic with visible bands-2, 3, and 4 having a medium reflectance value
- The band-6 (SWIR1), on the other hand, has typical reflectance with a differentiation characteristic between the lithological rock groups described by the study area. Band-7 (SWIR2) also has a high absorption rating (Fig. 6a and b)
- The spectral properties of Neoproterozoic rocks of the study area have a few different characteristics around bands 2 and 3, with an emphasized reflectance feature around bands 5 and 7 and typical differences in reflectance features for band 6
- Neoproterozoic rocks represented by gneiss-amphibolite-schist, granitic gneiss, tonalite, diorite, granodiorite, granite G1, Dokhan volcanic, granites G2 and G3, pyroclastic breccia, and tertiary dikes reveal that maximum reflectance occurs at 1.609 μm of the SWIR region of band 6 and the minimum reflectance at 0.4826 μm of the visible region of band 2, except for tonalite and granite G3, where the minimum
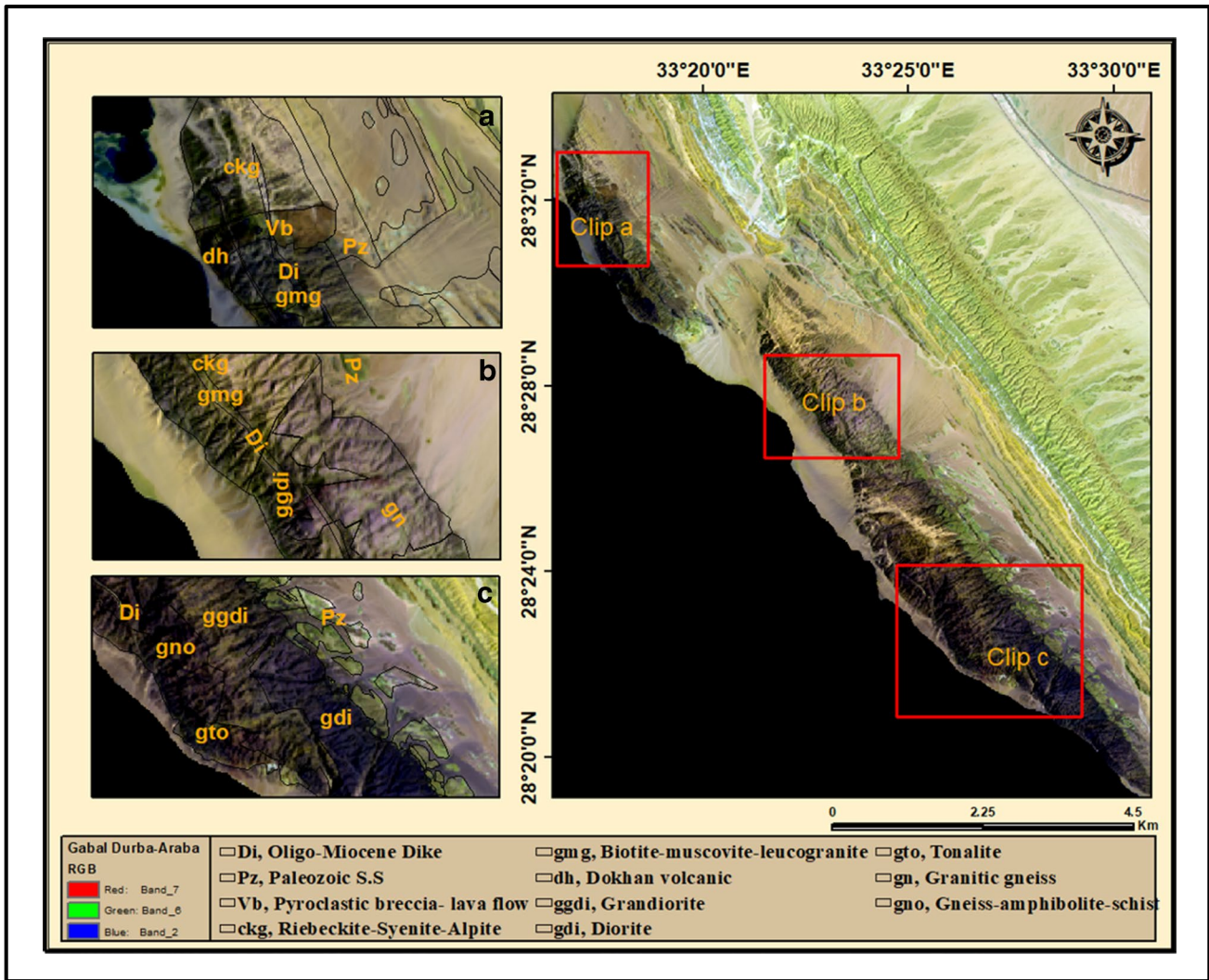
Fig. 4 The study area and clipping of **a** Gabal Ab Durba; **b** Gabal Abu Haswa; **c** Gabal Araba and its characterized rock units including Dokhan volcanic, different types of granites, volcanic breccia, and dikes shown in false color 7, 6, 2 RGB

reflectance (0.5613 μm) occurs at the VINR region of band 3 (Table 5)

- Tonalite, diorite, Dokhan volcanic, and granite G3 show a low differentiation between VINR, NIR, and SWIR electromagnetic waves (Fig. 6a and b)
- The maximum reflectance can be used as the denominator or numerator to differentiate lithological rock units of the study area (e.g., 7/6, 6/7, 6/5, 6/4, 2/6, 5/6, 5/4, 4/6, 4/3, 5/7, 4/5, 4/2, 3/2, 6/5).

Based on the spectrum reflectance profiles and previous research (Fig. 6a and b), various images were derived and powerfully tested to define the best BR in the proposed lithological units in the study area (e.g., 3/4, 4/6, 2/1 RGB, 7/6, 2/6, 5/6 RGB, and 5/2, 3/2, 7/2 RGB).

Material identification

Many spectral matching algorithms, ranging from the traditional clustering techniques to more recent automated matching models, have evolved (Shanmugam and Srinivasaperumal 2014). Comparing it to every signature in THOR-integrated spectral libraries, THOR tools automatically compute the correct scale factor required to scale the unknown signature to the same scale as reflectance libraries. Libraries in THOR include the Imaging Spectrometer Data Analysis System (ISDAS), developed by the Canadian Centre for Remote Sensing in 1995, and the USGS's Tricorder (Clark et al. 1990). These systems provide basic data input and output, interactive display, and data analysis for imaging spectrometers. Single algorithms, such as SAM in SIPS,
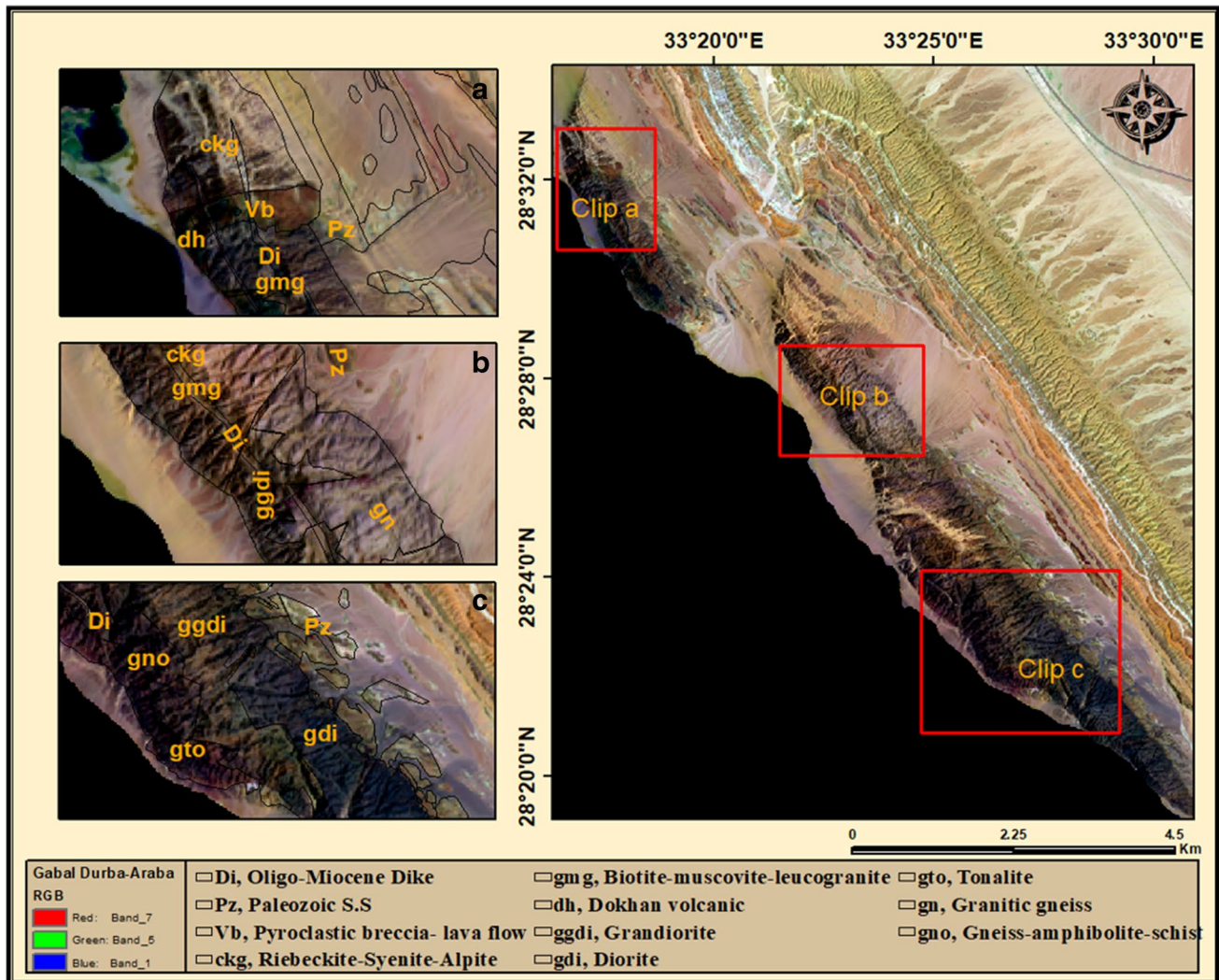
Fig. 5 The study area and clipping of **a** Gabal Abu Durba, **b** Gabal Abu Haswa, **c** Gabal Araba and its characterized rock units including Dokhan volcanic, different type of granites, volcanic breccia, and dikes shown in false color 7, 5, 1 RGB

SFF in Tricorder, and MRSFF in Tetracorder, govern spectral matching for most mineral mapping applications (Shanmugam and Srinivasaperumal 2014). The matching results are sorted with the best matches on top (the smaller spectral angels are good (less than 0.08), fair (0.081–014), poor (0.1141–0.25), and very poor (greater than 0.251) (Material Identification 2021). In this study, the THOR technique was used to detect and recognize different rock unit samples classified as BR 3/4, 4/6, 2/1 RGB, 7/6, 2/6, 5/6 RGB, and 5/2, 3/2, 7/2 RGB, and the results were compared with previous geological mapping of the study area and then used as ground trust ROI for supervised classification.

Supervised classification

Supervised classification requires a significant amount of input from an image analyst and information about the sorts of surfaces observed in the study area. This information may be collected through maps or fieldwork, in which various surface classes are recognized and then entered into the software as ROI. It can also be achieved by collecting end members or acquiring a unique spectrum for each rock segment. Various supervised categories, including classifications based on Mahalanobis distance and maximum likelihood, were tested.

Results

Various remote-sensing image-processing techniques were employed in this study. They are categorized as follows:

a) Color composite images

Fig. 6 Spectral signature analysis of exposed rock units of the study area showing the reflectance feature of different Landsat-8 bands
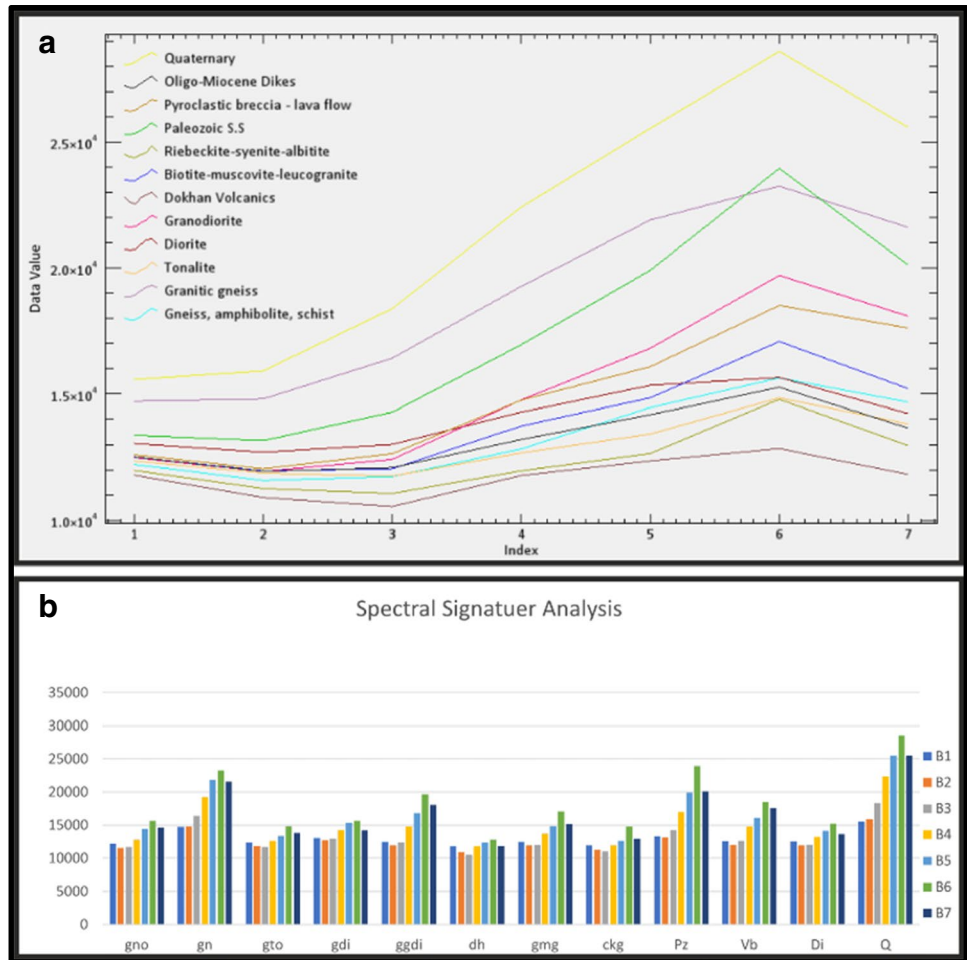
The statistical OIF technique was used to pick the most informative color image from the Landsat-8 band composite images. The best band composite image was chosen with a high percentage to extract useful information about the land surface, such as hydrothermally spectral analyst discrimination (Table 4). Band composite images 7, 6, 2 RGB and 7, 5, 1 RGB are more varied and suitable for the rock units in the study area and

provide an excellent base map in which rock units are easily discriminated (Figs. 4 and 5).

b) Band ratio

In this study, various BRs were prepared from Landsat-8 OLI data based on spectral signature analysis and earlier band reports approved in the publication. BR

Table 5 The wavelength and reflectance values of Landsat-8 seven bands characterized for each of rock units in the study area in the range VNIR and SWIR

| Bands	Wavelength	Reflectance Values										
		gno	gn	gto	gdi	ggdi	dh	gmg	ckg	Pz	Vb	Di	Q
B1	0.443	12210	14722	12352	13042	12481	11784	12505	11971	13369	12596	12509	15577
B2	0.4826	11573	14808	11865	12696	11932	10896	11953	11256	13155	12037	11937	15917
B3	0.5613	11727	16422	11747	13004	12411	10540	12042	11058	14281	12639	12084	18389
B4	0.6546	12827	19273	12670	14282	14767	11772	13733	11956	16957	14759	13201	22413
B5	0.8646	14466	21902	13414	15347	16815	12350	14853	12645	19909	16084	14179	25538
B6	1.609	15640	23245	14852	15659	19705	12842	17083	14794	23950	18516	15272	28586
B7	2.201	14680	21606	13813	14222	18088	11815	15212	12955	20111	17618	13648	25570
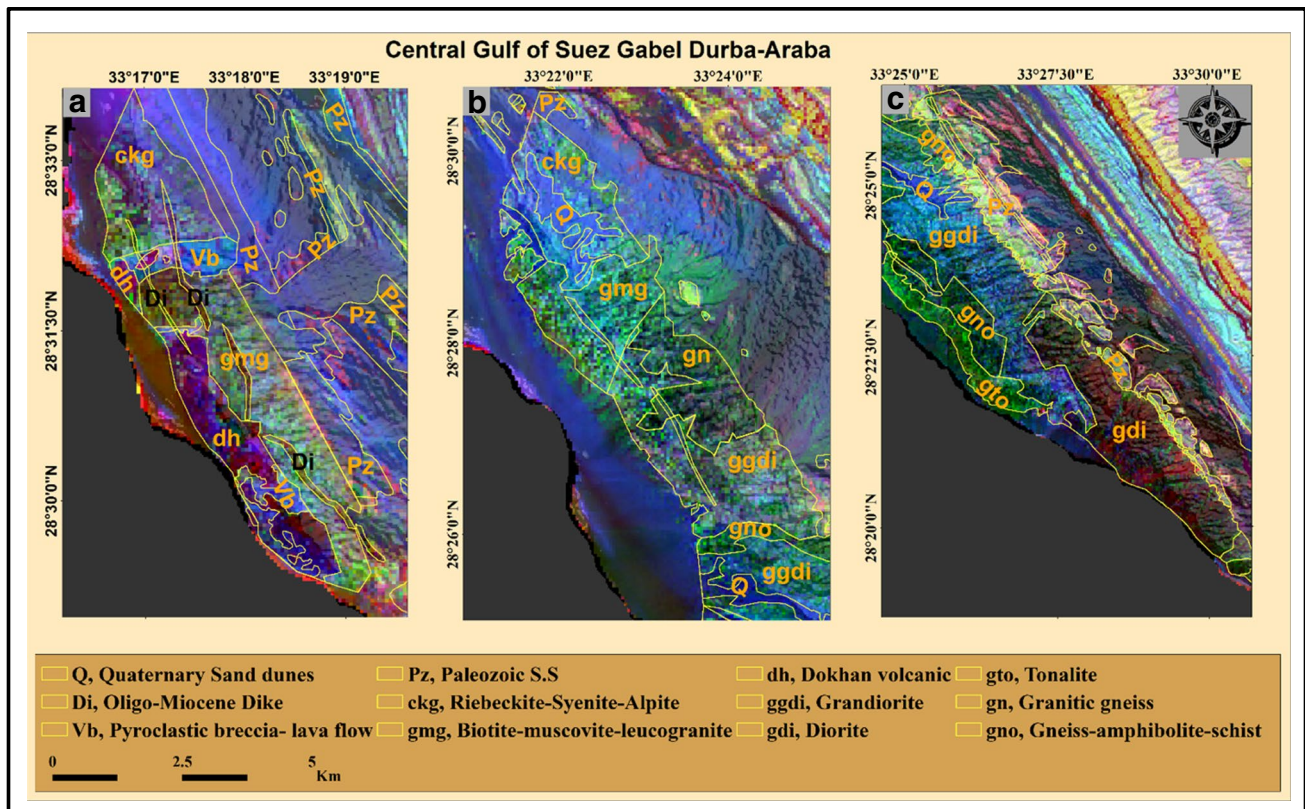
Fig. 7 Zeinelabdein Band ratio 6/7, 6/4, 4/2 RGB of Landsat-8 image showing **a** Gabel Abu Durba, **b** Abu Haswa, **c** Gabel Araba and its characterized rock units

was employed because it can provide high contrast and differentiate among the various lithological rock units that characterize the study area. Landsat-8 intruded by Zeinelabdein et al. (2014) delineates Gossanic ridges in the Red Sea State of Khartoum associated with gold mineralization based on Landsat-8. In the investigation at Gabal Abu Durba, Precambrian basement rock is distinguished as Dokhan volcanic (dh), which is violet; granite G2, biotite-muscovite-leucogranite (gmg); and granite G3, riebeckite-syenite-albitite (ckg), which is green. A light blue region appears in pyroclastic breccia and lava flow (vb), whereas an olive region is featured in tertiary dike (Di) trending NW (Fig. 7a). In Gabal Abu Haswa, there is no difference between the various types of granite as they are all characterized by a green hue, whereas the granitic gneiss district is deep green (Fig. 7b). Gabal Araba is classified into four categories of granitoids (granite G1) with high sharp contact between different lithological units, where the gneiss-amphibolite-schist (gno) is depicted in deep green; tonalite (gto) appears in green, diorite (gdi) in deep red, and granodiorite in blue (Fig. 7c). In lithological differentiation of the east Esh El Malaha area south of the Gulf of Suez, Egypt, Seleim and Hammed (2016) employed two BRs, including 3/4, 4/6,

2/1 RGB and 7/6,2/6, 5/6 RGB (Figs 8 and 9). Using the first BR, 3/4, 4/6, 2/1 RGB, the Precambrian basement in Gabal Abu Durba is categorized as Dokhan volcanic (dh), which is green; granite G2, biotite-muscovite-leucogranite (gmg), which shows in saddle brown; and granite G3, riebeckite-syenite-albitite (ckg), which shows in brown. A green region appears in pyroclastic breccia and lava flow (vb), whereas goldenrod is featured in tertiary dike (Di) trending NW (Fig. 8a). Gabal Abu Haswa is classified into three: granitic gneiss with a pale-yellow hue, granite G2 with biotite-muscovite-leucogranite (gmg), and granite G3 with riebeckite-syenite-albitite (ckg), which is violet (Fig. 8b). Gabal Araba is categorized into four granitoids (granite G1) with high sharp contact between different lithological units. These include gneiss-amphibolite-Schist (gno), depicted in green-yellow, tonalite (gto) in orange, diorite (gdi) in yellow, and granodiorite (gg) (Fig. 8c). The second BR image, 7/6, 2/6, 5/6 RGB (Fig. 9), shows a good result with clear differences in nearly all rock type boundaries in the study area. Gabal Abu Durba is categorized as Dokhan volcanic (dh), which has a pale-blue hue; granite G2, biotite-muscovite-leucogranite (gmg), with dark goldenrod; and granite G3, riebeckite-syenite-albitite (ckg), which
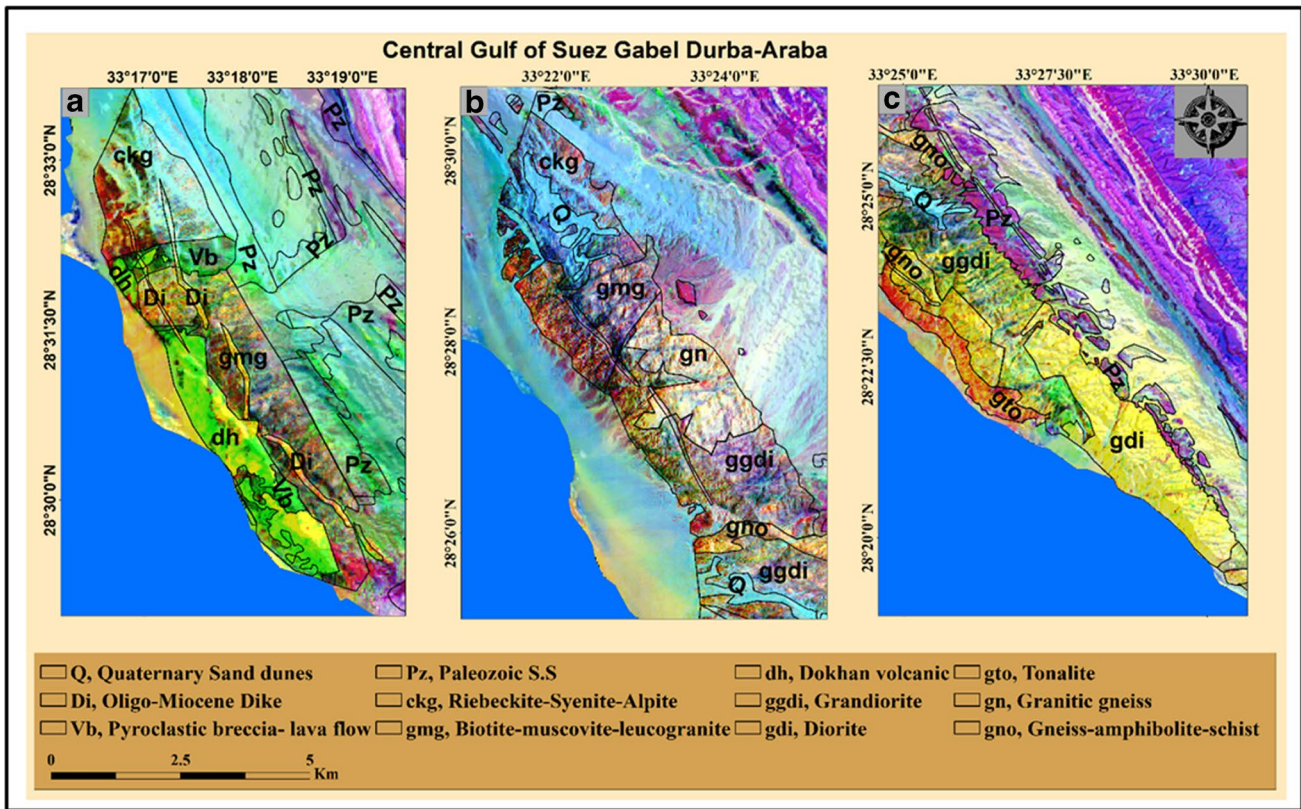
Fig. 8 Seleim Band ratio 7/6, 2/6, 5/6 RGB of Landsat-8 image showing **a** Gabel Abu Durba, **b** Abu Haswa, **c** Gabel Araba and its characterized rock units

is brown. Pyroclastic breccia and lava flow (vb) are red, whereas tertiary dike (Di) seems light (Fig. 9a). Gabal Abu Haswa is classified into three: granitic gneiss with a buff hue, granite G2 with biotite-muscovite-leucogranite (gmg), and granite G3, riebeckite-syenite-albitite (ckg) with a pale-orange hue (Fig. 9b). Neoproterozoic in Gabal Araba is classified into four categories of granitoids (granite G1) with high sharp contact between different lithological units. The gneiss-amphibolite-schist (gno) appears in pale-yellow, tonalite (gto) in orange, diorite in white, and granodiorite in pink (Fig. 9c). BR provided by the spectral signature analyzers of OLI data 5/2, 3/2, 7/2 RGB discriminates acidic, basic, and intermediate granitoid rocks (Fig. 10). The BR divides the Neoproterozoic rocks of Abu Durba into two rock units, including acidic rock, which appears violet, and basic rock, which is deep red, and basic dikes appear black (Fig. 10a). Gabal Abu Haswa is categorized as acidic; granite G2 biotite-muscovite-leucogranite; and granite G3, riebeckite-syenite-albitite (ckg), which is violet, whereas the granitic gneiss is green (Fig. 10b). Gabal Araba is classified into four granitoid categories (granite G1) with low contact between different lithological units. Gneiss-amphibolite-schist (gno) appears green, tonalite

(gto) appears blue, diorite (gdi) appears black, and granodiorite (ggdi) appears violet, and there is no clear contact (Fig. 10c).

iii) Material Identification (THOR)

By comparing the spectral signatures of unknown rocks in the study area to the spectral database using THOR, we discovered that the northern part of Gabal Durba is characterized by alkalic syenite granite G3 with reference matching of 0.0684 (Fig. 11a) and the eastern part is characterized by Muscovite granite G2 with reference matching of 0.0657 (Fig. 11b), whereas the western part is characterized by muscovite granite G2 with reference matching (Fig. 11c and d). Furthermore, the northern section of Gabal Abu Haswa contains alkalic synite granite G3 with a reference matching 0.0771 (Fig. 11e), whereas the eastern part is composed of granite gneiss with a reference matching 0.0509 (Fig. 11f).

iv) Supervised classification

Maximum-likelihood and Mahalanobis distance classifications were employed for supervised categorization of the optimal lithological classification (Fig. 12a, b). The training data were chosen based on the image transformation, which included the selected BRs of 6/7, 6/4, 4/2 RGB, 3/4, 4/6, 2/1 RGB, 7/6, 2/6, 5/6 RGB, and 5/2, 3/2, 7/2 RGB of
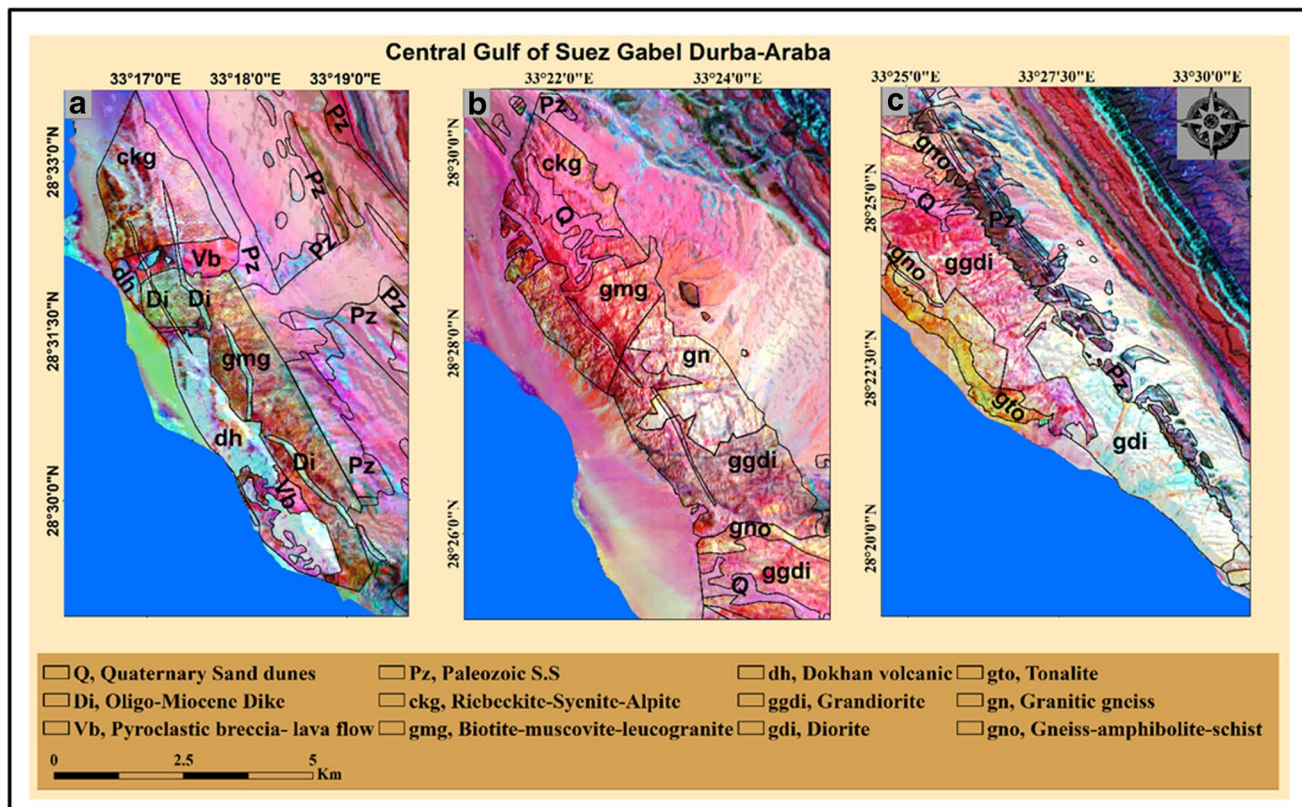
Fig. 9 Seleim Band ratio 7/6, 2/6, 5/6 RGB image showing **a** Gabel Abu Durba, **b** Abu Haswa, **c** Gabel Araba and its characterized rock units

OLI data that can discriminate the main basement rock units of Gabal Durba, Abu Haswa, and Gabal Araba, where the ROI was selected. Using ground trust ROI, accuracies of 86.6% and 75.7085% were obtained for the maximum likelihood and Mahalanobis classifications with kappa values of 0.8634 and 0.7192, respectively, through confusion matrix classification. The maximum probability and Mahalanobis classification categorize the rock units of Gabal Durba, Abu Haswa, and Gabal Araba with high sharp contact. The Gabal Araba granite is classified into four granitoid varieties, including gneiss-amphibolite schist, Tonalite, diorite, and granodiorite. Gabal Abu Haswa is divided into granitic gneiss, biotite-muscovite-leucogranite, and riebeckite-syenite-albitite. Gabal Abu Durba is categorized into Dokhan volcanic, biotite-muscovite-leucogranite, riebeckite-syenite-albitite, tertiary volcanic, and basaltic dike, and Paleozoic S.S uncomfortably rests on the tilted basement blocks from the west of Gabal Araba and Gabal Abu Durba (Fig. 12a, b).

Discussion

The study area, located on the eastern edge of the central Gulf of Suez rift, exposes elongated basement blocks of Gabal Durba–Abu Haswa and Araba. Previous research has been limited to field surveys, chronology, and chemical analysis (e.g., Egyptian Geological Survey 1994 Fig. 13 a; El-Bialy 1999; Anbar et al. 2005) or remote-sensing techniques (e.g., Geological and Survey 2015: Fig. 14). To compare distinct lithological rock units, both approaches give low-resolution geological maps. In the study area, Landsat-8 data preprocessing and remote-sensing technology interpretations for building BRs for enhanced lithological-unit categorization are effective. All three tested BR combinations could separate at least the principal exposed rock segments in previous research. Two of the combinations, including BR 3/4, 4/6, 2/1 RGB and 7/6, 2/6, 5/6 RGB of Seleim and Hammed (2016), showed the best results. In particular, BR 6/7, 6/4, and 4/2 RGB of Landsat-8 intruded by Zeinelabdein et al. (2014) gained an acceptable contrast and good separability between different types of older granite and Dokhan volcanic, but it could not divide the various types of younger granite. BR 5/2, 3/2, and 7/2 RGB could discriminate between basic, intermediate, and acidic rocks. All tested BR combinations described in previous studies and extracted according to spectral signature analysis could separate at least the primary exposed rock units (e.g., gneiss-amphibolite-schist, granitic gneiss, granite G1, Dokhan volcanic, granite G2, and granite G3, Pyroclastic breccia, and tertiary dikes). The methods used to process and analyze Landsat-8 images could divide rock units in the study area more
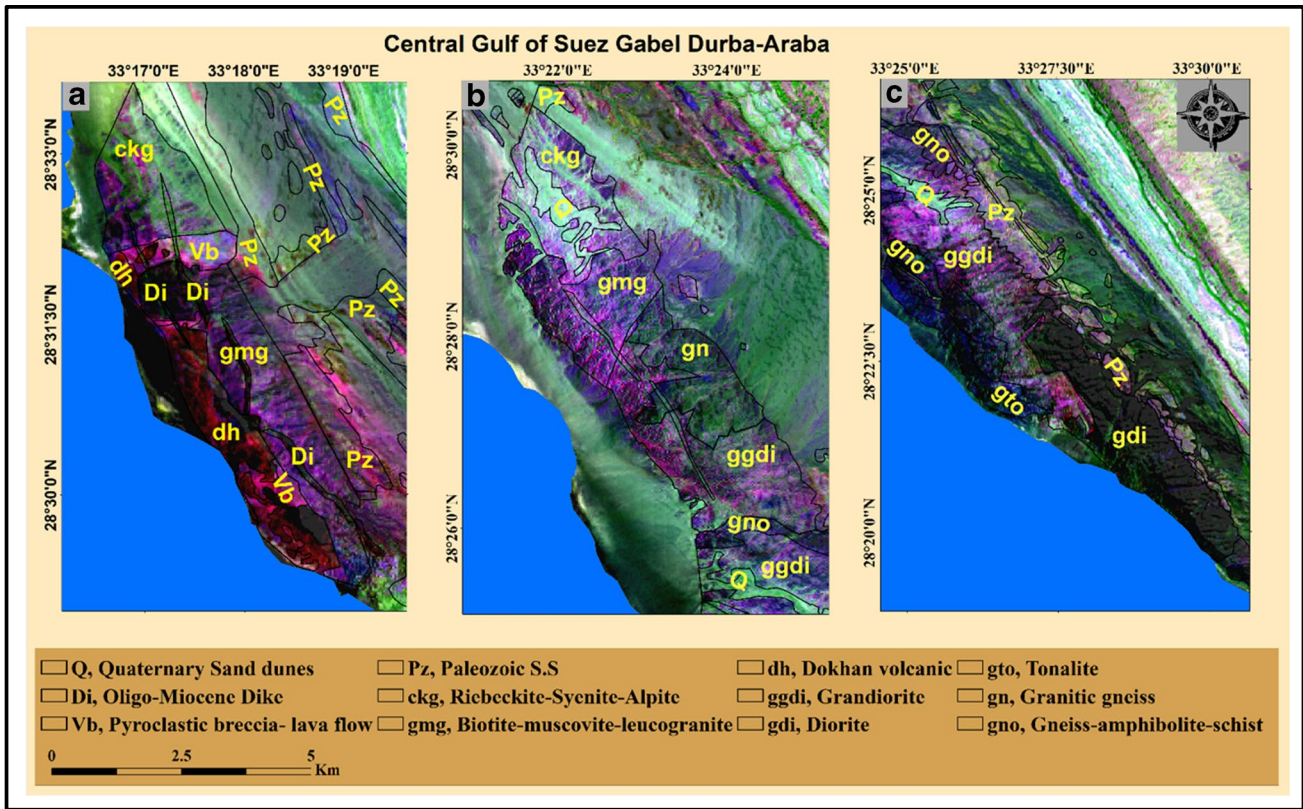
Fig. 10 Band ratio 5/2, 3/2, 7/2 RGB of Landsat-8 image showing **a** Gabel Abu Durba, **b** Abu Haswa, **c** Gabel Araba and its characterized rock units

accurately to improve the identification of lithological units. In addition, THOR techniques were effective in identifying the same rock units that are disputed in the study area.

We compare our results with those of previous studies in three sections:

1. Gabal Durba is a single geological block that comprises granite G3 (Egyptian Geological Survey 1994), and it is divided into three geological units: Dokhan volcanic on the western side, granite G2 on the eastern side, and granite G3 on the northern side (El-Bialy 1999 and Anbar et al. 2005). Pyroclastic and lava flows occur only on the western side of Gabal Abu Durba, principally as a relatively large mass of liver-like shape in addition to other minor smaller bodies (El-Bialy 1999). Geological Survey (2015) reported that Gabal Abu Durba has two rock units: granite G2 and volcanic breccia intruded by tertiary dikes. BR images were used in this study. 6/7, 6/4, 4/2 RGB (Fig. 7) after Zeinelabdein et al. (2014) and 3/4, 4/6, 2/1 RGB (Fig. 8) and BR 7/6, 2/6, 5/6 RGB (Fig. 9) after Seleim and Hammed (2016) showed that the Gabal Abu Durba is classified into four rock units with clear contact: the eastern part is identified as granite G2, the western part as Dokhan volcanic, and the most eastern part as granite

G3, which is introduced by tertiary dikes. Also, pyroclastic and lava flow occur only on the western side. This is contrary to the findings of the Geological Survey (2015). Thus, there is a need to define the kind of rock units using a THOR material identification approach, which revealed that most parts of the western side of Gabal Durba are characterized by Dokhan volcanic rocks with rhyolitic and basaltic andesite compositions (Fig. 11c, d). Furthermore, the most northern portion is distinguished by granite G3 alkali syenite (Fig. 11a) and the eastern part by granite G2 muscovite composition.

2. To the south, the Neoproterozoic of Gabal Abu Haswa contains granitic G2 (El-Bialy 1999), which is divided into two groups: granite G2 and G3 (Egyptian Geological Survey 1994 and Anbar et al. 2005). However, it was classified as granitic gneiss by the Geological Survey (2015). BR 3/4, 4/6, 2/1 RGB and 7/6, 2/6, 5/6 RGB revealed three distinct contacts between rock units, including granitic gneiss, granite G2, and granite G3. El-Bialy (1999) reported that both gneissose and large granites are exposed at the west of Gabal Abu Haswa where they exhibit somewhat dispersed contact, which contradicts the results obtained here. BR 3/4, 4/6, 2/1 RGB and 7/6, 2/6, 5/6 RGB showed that granitic gneiss located at the eastern
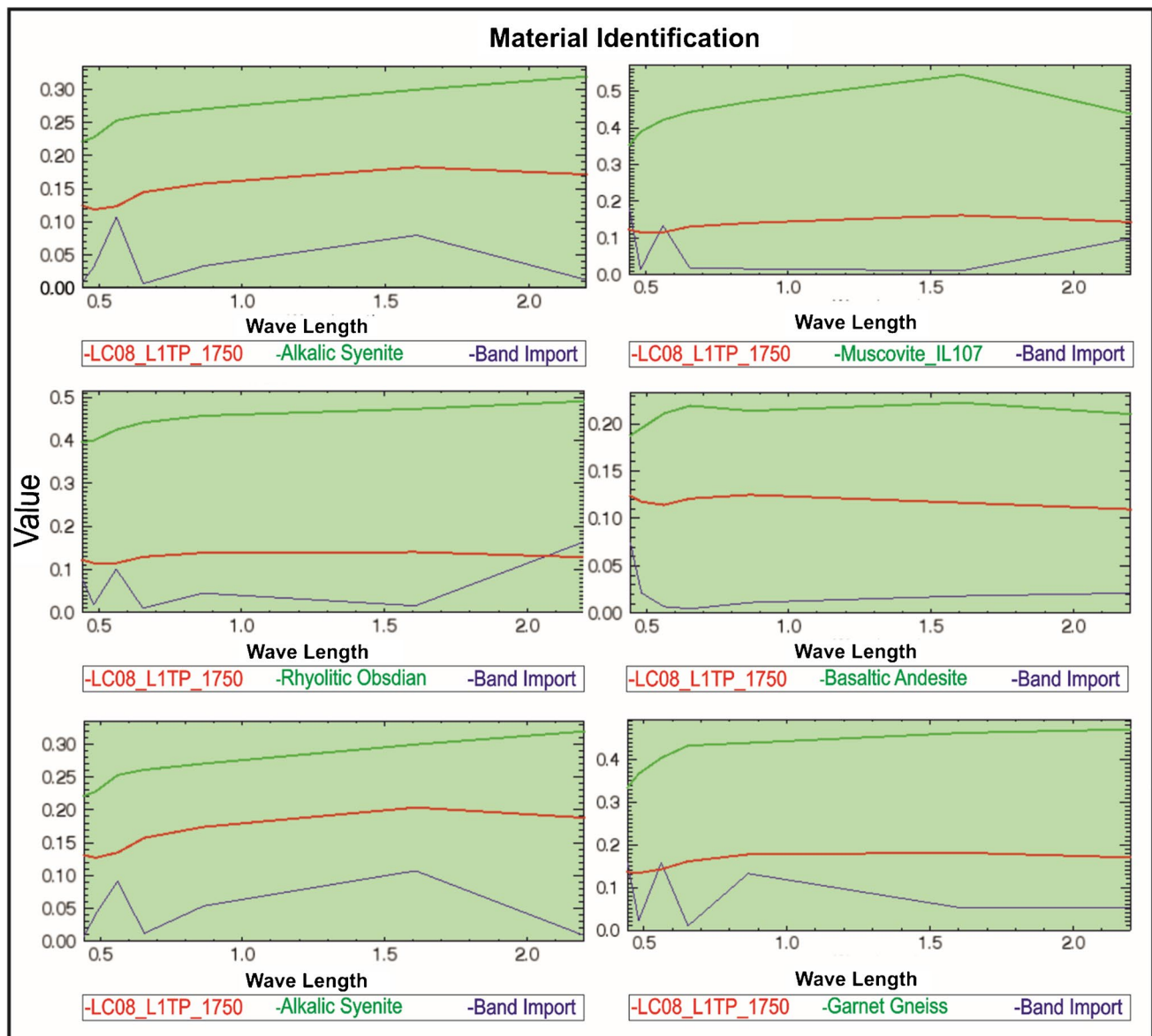
Fig. 11 THOR material identification of **a** granite G3 (alkalic syenite) in the northern part of Gabal Abu Durba; **b** granite G2 (muscovite) at the eastern part; **c, d** Dokhan volcanic at the western part (rhyolite and basaltic andesite); **e** granite G3 at the northern part of Gabal Abu Haswa (alkalic syenite); **f** granitic gneiss of Gabal Abu Haswa

side is mostly occupied by gneiss. The BR 5/2, 3/2, and 7/2 RGB images also divide the Abu Haswa basement into two rock units shown in green and violet. The THOR material identification approach revealed that the green rock unit is a granitic gneiss (Fig. 11f).

3. Moving south of Gabal Araba, the Egyptian Geological Survey (1994) and Geological Survey (2015) categorized Araba basement rocks into gneisses, migmatites, and amphibolite; granite G1; and granite G2, with differences in contact among the rock groups (Figs. 13a and 14). 6/7, 6/4, 4/2 RGB, BR 3/4, 4/6, 2/1 RGB, and 7/6, 2/6, 5/6 RGB showed clear contact between several rock units in

Gabal Araba where the rock unit contact has been reclassified (e.g., tonalite diorite and granodiorite: Fig. 13b).

Following the selection of training data, THOR material identification was effective for the supervised classification process, giving the overall best classification accuracy. The prepared lithological map shows clear improvements and variations from the earlier version. Generally, many predicted borders between the lithological units were set up newly, and others were confirmed. Also, the discrimination between several rock types was enhanced, e.g., the granitic gneiss of Gabal Abu Haswa and the Dokhan volcanic of
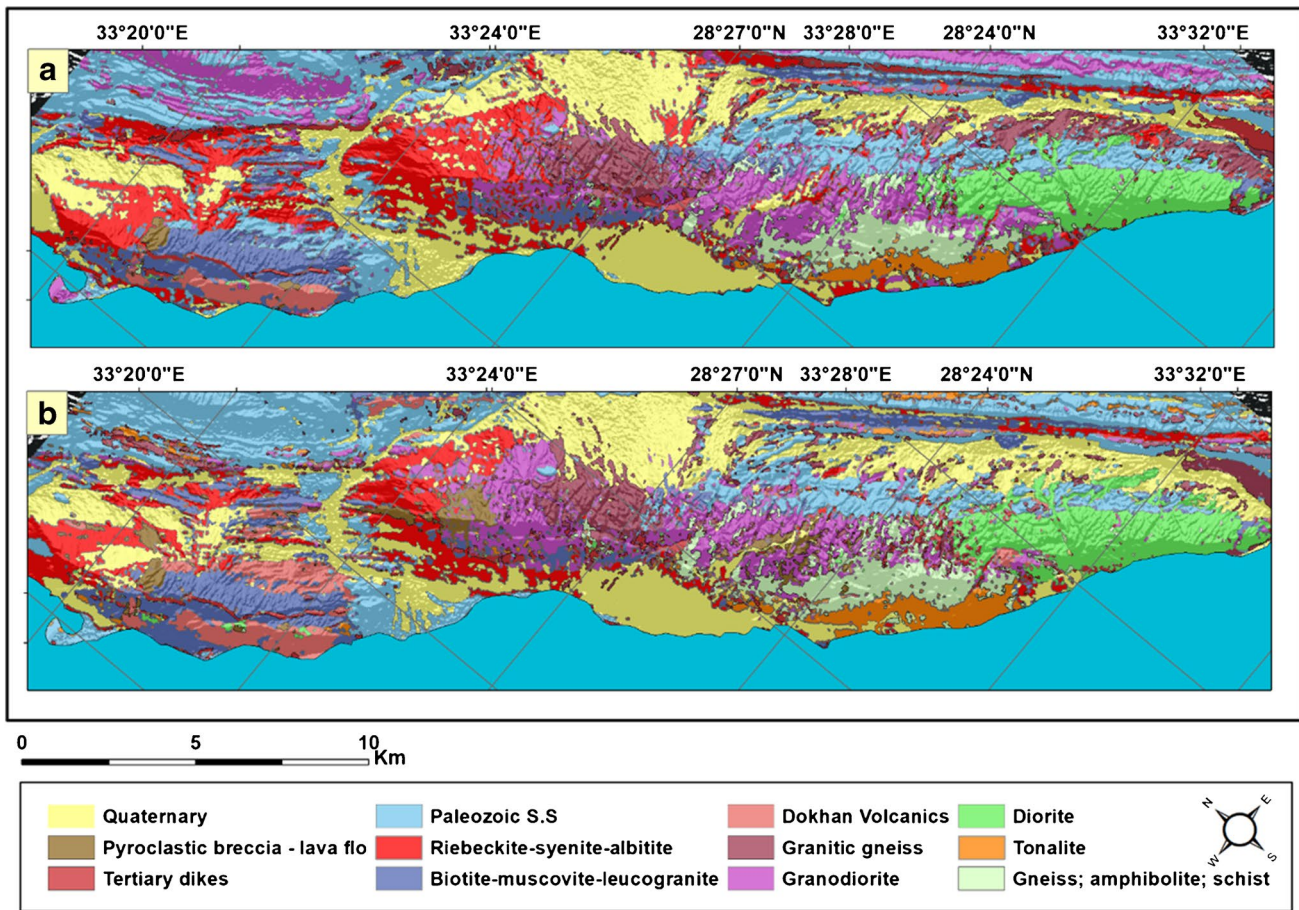
Fig. 12 Supervised classifications. **a** Maximum likelihood. **b** Mahalanobis distance classification

Gabal Abu Durba. Even though the results are satisfactory, some regions in the study area show vague results. Classifications, such as confusion between granitoid and biotite-muscovite-leucogranite at Gabal Abu Haswa, also classified Paleozoic S.S as Dokhan volcanic at the eastern part of Gabal Abu Durba. Herein, additional field data would be needed to define further training areas for lithological units. Combining the classification results with field verification, a new lithological map could be created (Fig. 13b).

Conclusions

In this study, we employed specific data processing techniques on Multispectral Landsat-8 datasets for the automated lithological classification of the study area. The proposed workflow resulted in a derivative dataset with enhanced information relevant for lithological discrimination of Neoproterozoic rock in Gabal Durba, Abu Haswa, and Gabal Araba. Most geological studies on the study area depend on the published traditional geological maps developed based on sample collection, geochronological, and geochemical processes. Due

to the difficulty in the geographic location, sharp topography, and inaccessibility to all places, geological maps of limited accuracy have been developed.

In this study, we employed OIF, a spectral signature analyst; image transformation generated from spectral band rationing; THOR material identification; and ultimately supervised classification. These techniques, in conjunction with previous geological mapping, were employed to update the geological map of the studied area. The revised lithological map (Fig. 13bb) shows more distinct improvements and variances than the previous map. The proposed workflow resulted in higher-resolution maps with accurate rock unit boundaries. Many lithological units have a new set of borders, whereas others are retained. Some rock units are subdivided into smaller and separate units (e.g., the granitoid of the Gabal Araba is divided into four phases, and the granitoids of Gabal Abu Haswa and Gabal Abu Durba are divided into three phases). Despite the high-accuracy assessment results of this study (kappa values 0.7192–0.8634), further field mapping would be useful to establish the rock variations as new classes. Since there is no comprehensive detailed field mapping for large regions, the new geological map cannot
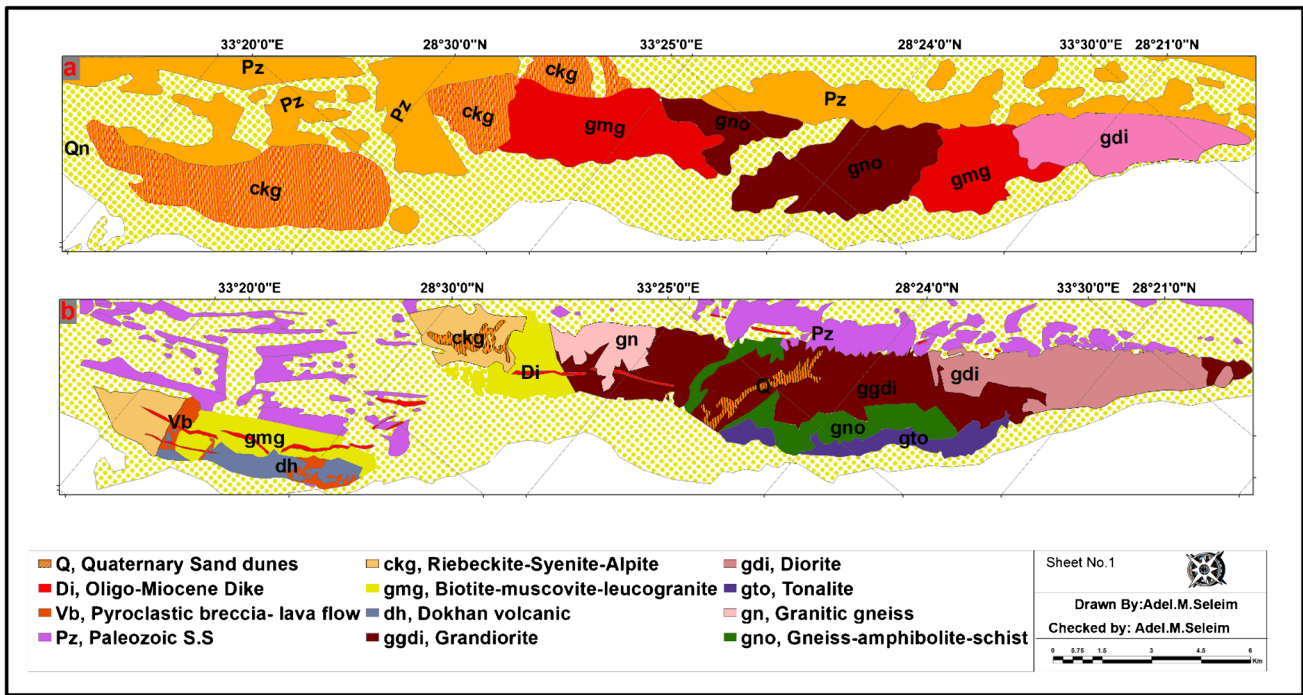
Fig. 13 Comparison between **a** Egypt Geological Map 1994, scale 1:250,000 above and below; **b** new lithological map of this study
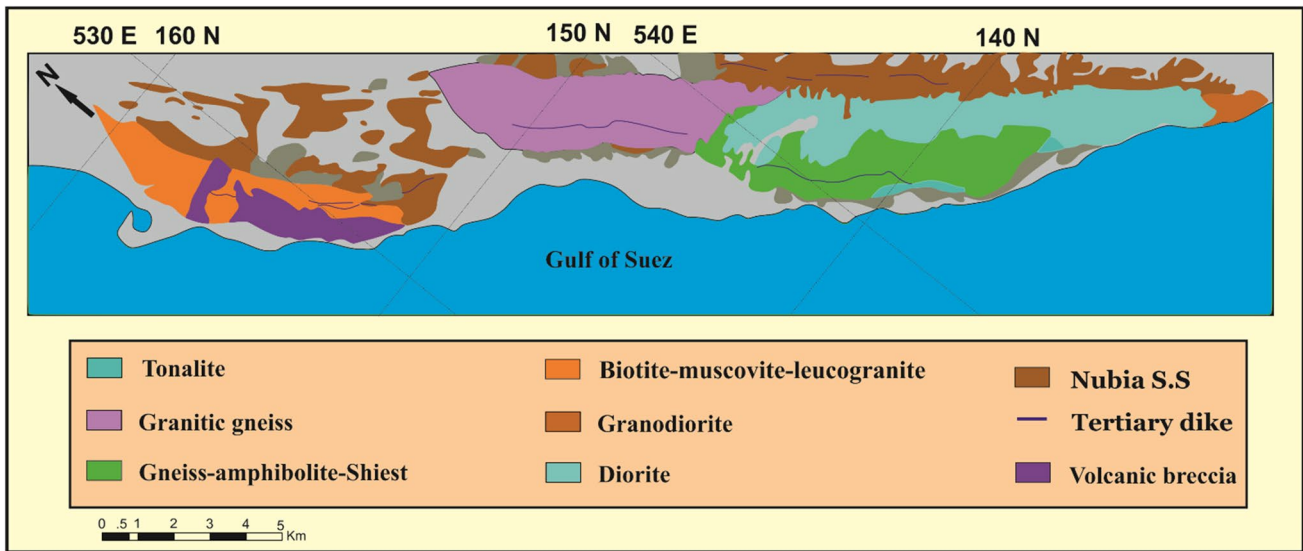

Fig. 14 Geological map of Precambrian rocks of South-West Sinsi, Egypt. Scale 1:75,000 illustrates different lithological rock units of the study area

guarantee 100% accuracy for some places. However, with a few exceptions, the findings are considered safe due to the high classification quality and outstanding outcomes. Final confirmation of this result can only be obtained by extending the field mapping to locations not previously studied.

Declarations

Competing interests The authors declare no competing interests.

References

Abdallah AM, El-Adindani A (1963) Notes on the Cenomanian-Turonian contact in the Galala Plateau, Eastern Desert. Egypt Egypt J Geol United Arab Repub 7:67–70

Abdel Kawy WAM, Abou El-Magd IH (2013) Use of satellite data and GIS for assessing the agricultural potentiality of the soils South Farafra Oasis, Western Desert. Egypt Arab J Geosci 6:2299–2311. https://doi.org/10.1007/s12517-012-0518-5

Abdelaal A, Sultan M, Elhebiry M et al (2021) Integrated studies to identify site-specific parameters for environmentally benign mining operations: a case study from the Sukari Gold Mine. Egypt Sci Total Environ 750:141654. https://doi.org/10.1016/j.scitotenv.2020.141654

Abdelkareem M, Gaber A, Abdalla F, El-Din GK (2020) Use of optical and radar remote sensing satellites for identifying and monitoring active/inactive landforms in the driest desert in Saudi Arabia. Geomorphology 362:107197

Abdelkareem M, Hamimi Z, El-Bialy MZ et al (2021) Integration of remote-sensing data for mapping lithological and structural features in the Esh El-Mallaha area, west Gulf of Suez, Egypt. Arab J Geosci 14 https://doi.org/10.1007/s12517-021-06791-3

Abu El-Leil I, Soliman NMA, Bekiet MH, Elhebiry MS (2019) Enhancing multispectral remote sensing data interpretation for historical gold mines in Egypt: a case study from Madari gold mine. Arab J Geosci 12:1–10

Al-Nahmi F, Alami OB, Baidder L et al (2016) Using remote sensing for lineament extraction in Al Maghrabah Area-Hajjah, Yemen. Int Arch Photogramm Remote Sens Spat Inf Sci 42:137

Anbar MMA, El-Naggar WSA, El Nahas AA, Darwish MM (2005) Geology and petrology of Abu Durba-Abu Haswa granitoid rocks, southwestern Sinai. Egypt Delta j Sci 29:136–155

Asran AM, Hassan SM (2021) Remote sensing-based geological mapping and petrogenesis of Wadi Khuda Precambrian rocks, South Eastern Desert of Egypt with emphasis on leucogranite. Egypt J Remote Sens Sp Sci 24:15–27. https://doi.org/10.1016/j.ejrs.2019.07.004

Azer MK (2006) The petrogenesis of late Precambrian felsic alkaline magmatism in South Sinai. Egypt Acta Geol Pol 56:463–484

Beiranvand Pour A, Park T-YS, Park Y et al (2018) Application of multi-sensor satellite data for exploration of Zn-Pb sulfide mineralization in the Franklinian Basin, North Greenland. Remote Sens 10:1186

Chrysoulakis N, Abrams M, Feidas H, Arai K (2010) Comparison of atmospheric correction methods using ASTER data for the area of Crete, Greece. Int J Remote Sens 31:6347–6385

Clark RN, Gallagher AJ, Swayze GA (1990) Material absorption band depth mapping of imaging spectrometer data using a complete band shape least-squares fit with library reference spectra. In: Proceedings of the Second Airborne Visible/Infrared Imaging Spectrometer (AVIRIS) Workshop pp 176–186

Cooley T, Anderson GP, Felde GW et al (2002) FLAASH, a MODTRAN4-based atmospheric correction algorithm, its application and validation. In: IEEE international geoscience and remote sensing symposium, pp 1414–1418

Crosta AP (1989) Enhancement of landsat thematic mapper imagery for residual soil mapping in SW Minais Gerais State, Brazil: a prospecting case history in Greenstone belt terrain. In: Proceedings of the Seventh thematic conference on remote sensing for exploration geology, 2–6 October, Calgary, Canada, 1989, pp 1173–1187

Drury SA, Walker ASD (1987) Display and enhancement of gridded aeromagnetic data of the Solway Basin. Int J Remote Sens 8:1433–1444

Egyptian Geological Survey and Mining Authority EGSMA (1994) Geological Map of Sinai, Arab Republic of Egypt (Sheet No.1) Scale 1:250,000. Cairo, Egypt

El-Bialy MZ (1999) Geology of the basement rocks of Abu Durba-Abu Haswa area, southwestern Sinai, Egypt. Unpubl M Sc thesis, Suez Canal Univ Ismailia, Egypt, p 189

El-Din GK, Abdelkareem M (2018) Integration of remote sensing, geochemical and field data in the Qena-Safaga shear zone: implications for structural evolution of the Eastern Desert. Egypt J African Earth Sci 141:179–193

Elhebiry MS, Sultan M, Abu El-Leil I et al (2020) Paleozoic glaciation in NE Africa: field and remote sensing-based evidence from the South Eastern Desert of Egypt. Int Geol Rev 62:1187–1204. https://doi.org/10.1080/00206814.2019.1636416

Eyal M, Hezkiyahu T (1980) Katherina pluton: the outline of a petrologic framework. Isr J Earth Sci 29:41–45

Gaber A, Amarah BA, Abdelfattah M, Ali S (2017) Investigating the use of the dual-polarized and large incident angle of SAR data for mapping the fluvial and aeolian deposits. NRIAG J Astron Geophys 6:349–360

Gad S, Kusky T (2007) ASTER spectral ratioing for lithological mapping in the Arabian-Nubian shield, the Neoproterozoic Wadi Kid area, Sinai. Egypt Gondwana Res 11:326–335

Geological M, Survey G (2015) Eyal M, Bentor YK, Eyal Y, Calvo R, Hall JK, Rosensaft M 2013b. Geological map of Precambrian rocks of South-West Sinsi, Egypt. Scale 1:75.000

Gharib ME, Obeid MA (2004) Geochemistry and evolution of the Neoproterozoic granitoid magmatism in the Wadi El-Sheikh-Gabal Saint Katherina area, Southwestern Sinai, Egypt. In: Proc 7th Int Conf on the Geology of the Arab World, Cairo University, pp 53–73

Ghrefat H, Kahal AY, Abdelrahman K et al (2021) Utilization of multispectral landsat-8 remote sensing data for lithological mapping of southwestern Saudi Arabia. J King Saud Univ - Sci 33:101414. https://doi.org/10.1016/j.jksus.2021.101414

Govender M, Chetty K, Bulcock H (2007) A review of hyperspectral remote sensing and its application in vegetation and water resource studies. Water Sa 33:145–151

Hamimi Z, Hagag W, Kamh S, El-Araby A (2020) Application of remote-sensing techniques in geological and structural mapping of Atalla Shear Zone and Environs, Central Eastern Desert, Egypt. Arab J Geosci 13:1–27

Hammed MS (2002) Geology and structural architecture of southwest Gulf of Suez, with special emphasis on the Precambrian rocks of

gebel el zeit area. Department of Geology, Faculty of Science, Cairo University Cairo-Egypt, Egypt, p 2002

Hassan SM, Sadek MF (2017) Geological mapping and spectral based classification of basement rocks using remote sensing data analysis: the Korbiai-Gerf nappe complex, South Eastern Desert. Egypt J African Earth Sci 134:404–418. https://doi.org/10.1016/j.jafrearsci.2017.07.006

Hassan SM, Sadek MF, Greiling RO (2015) Spectral analyses of basement rocks in El-Sibai-Umm Shaddad area, Central Eastern Desert, Egypt, using ASTER thermal infrared data. Arab J Geosci 8:6853–6865. https://doi.org/10.1007/s12517-014-1729-8

L3harrisgeospatial.com (2021b) Material identification. [online] available at<https://www.l3harrisgeospatial.com/docs/thormaterialidentification.html>; [Accessed 9 September 2021b].

L3harrisgeospatial.com (2021a) Fast Line-of-sight Atmospheric Analysis of Hypercubes (FLAASH). [online] Available at: <https://www.l3harrisgeospatial.com/docs/FLAASH.html#Before> [Accessed 5 September 2021a].

Loughlin WP (1991) Principal component analysis for alteration mapping. Photogramm Eng Remote Sensing 57:1163–1169

Matthew MW, Adler-Golden SM, Berk A, et al (2000) Status of atmospheric correction using a MODTRAN4-based algorithm. In: Algorithms for multispectral, hyperspectral, and ultraspectral imagery VI. 199–207

Montenat C, Ott D'Estevou P, Purser B et al (1988) Tectonic and sedimentary evolution of the Gulf of Suez and the northwestern Red Sea. Tectonophysics 153:161–177. https://doi.org/10.1016/0040-1951(88)90013-3

Morley CK (1995) Developments in the structural geology of rifts over the last decade and their impact on hydrocarbon exploration. Geol Soc London Spec Publ 80:1–32

Moustafa AM (1976) Block faulting in the Gulf of Suez EGPC., 5th Explor. Semin Cairo 19

Moustafa AR, El-Raey AK (1993) Structural characteristics of the Suez rift margins. Geol Rundschau 82:101–109. https://doi.org/10.1007/BF00563273

Omwenga B (2018) Use of space-borne imageries in mapping of hydrothermal alteration zones and geological structures in the Eburru Geothermal Complex, Kenya. 14. Kigali, Rwanda

Ourhzif Z, Algouti A, Hadach F (2019) Lithological mapping using landsat 8 oli and aster multispectral data in Imini-Ounilla district south high Atlas of marrakech. Int Arch Photogramm Remote Sens \& Spat Inf Sci

Patton TL, Moustafa AR, Nelson RA, Abdine SA (1994) Tectonic evolution and structural setting of the Suez Rift: Chapter 1: Part I. Type Basin: Gulf of Suez

Qaid AM, Basavarajappa HT (2008) Application of optimum index factor technique to Landsat-7 data for geological mapping of north east of Hajjah, Yemen. Am J Sci Res 3:84–91

RajanGirija R, Mayappan S (2019) Mapping of mineral resources and lithological units: a review of remote sensing techniques. Int J Image Data Fusion 10:79–106

Sabine C (1999) Remote sensing strategies for mineral exploration. Remote Sens Earth Sci Remote Sens 375–447

San BT, Sumer EO, Gurcay B (2004) Comparison of band ratioing and spectral indices methods for detecting alunite and kaolinite minerals using ASTER data in Biga region, Turkey. In: Proceedings ISPRS

Seleim AM, Hammed MS (2016) Applications of remote sensing in lithological mapping of east Esh El Malaha area, southwest Gulf of Suez. Egypt Int J Sci Eng Res 7:691–701

Shanmugam S, Srinivasaperumal P (2014) Spectral matching approaches in hyperspectral image processing. Int J Remote Sens 35:8217–8251

Shokry MM, Sadek MF, Osman AF, El Kalioubi BA (2021) Precambrian basement rocks of Wadi-Khuda-Shut area, South Eastern Desert of Egypt: geology and remote sensing analysis. Egypt J Remote Sens Sp Sci 24:59–75. https://doi.org/10.1016/j.ejrs.2019.12.005

Ungerer P, Bessis F, Chenet PY et al (1984) Geological and geochemical models in oil exploration; principles and practical examples

Zakeri H, Yamazaki F, Liu W (2017) Texture analysis and land cover classification of Tehran using polarimetric synthetic aperture radar imagery. Appl Sci 7:452

Zeinelabdein KAE, Halim A, El NH (2014) The use of Landsat 8 OLI image for the delineation of gossanic ridges in the Red Sea Hills of NE Sudan. Am J Earth Sci 1:62–67

Zhu Q, Abdelkareem M (2021) Mapping groundwater potential zones using a knowledge-driven approach and GIS analysis. Water 13:579